JETIR.ORG ISSN: 2349-5162 | ESTD Year : 2014 | Monthly Issue
JOURNAL OF EMERGING TECHNOLOGIES AND INNOVATIVE RESEARCH (JETIR)
An International Scholarly Open Access, Peer-reviewed, Refereed Journal

Impact of Morphology on Supercapacitor Performance of Nanostructured Molybdenum-, Tungsten-Disulfide and their composite with Polyaniline

Kavita Yadav[1], Nitika Mor[1] and Yashpal Sharma[2, a*)] and Jitendra Gangwar[3, b*)]

[1]*Department of Chemistry, Baba Mastnath University, Asthal Bohar, Rohtak, Haryana, 121021, India*

[2]*Department of Chemistry, RPS Degree College, Balana, Mahendergarh, Haryana, 123029, India*

[3]*Department of Physics, RPS Degree College, Balana, Mahendergarh, Haryana, 123029, India*

Abstract

This study explained three main thrusts, synthesis-morphology-application, of nanostructured molybdenum disulfide (MoS_2) and tungsten disulfide (WS_2) in details. The prime thrust is to provide a hydrothermal methodology, which is facile, environmentally begin and cost-effective synthesis approach, with understanding of formation mechanism of MoS_2 and WS_2 nanostructures. The second thrust is to express a deep insight into unique morphologies in 0D, 1D, 2D and 3D geometries exposing via various electron microscopy images of MoS_2 and WS_2 nanostructures. Additionally, synthesis and FT-IR characterization of Polyaniline (PANi), WS_2, and PANi-WS_2 composite are also described. To provide a supercapacitor performance with an impact of distinctive morphologies of MoS_2 and WS_2 nanostructures is the third thrust of this study. Finally, the important findings on both nanostructured MoS_2 and WS_2 demonstrated well here can lead to be promising potential materials in further supercapacitors applications.

Keywords

MoS_2, WS_2, Synthesis, Electron Microscopy, Supercapacitor

I. Introduction

Nowadays, energy crisis in terms of energy storage and energy conversion has aroused an extensive area of interest in the worldwide scientific and human communities [1-9]. Owing to the growing concerns and intrinsic tunable properties of transition metal dichalcogenides (TMDs) in nanoscience and nanotechnology, more and more TMDs extensively researched globally for energy storage devices and electrochemical applications such as supercapacitors, lithium-, sodium-, potassium- and magnesium-ion batteries, solar cells, hydrogen evolution and water splitting [3-8, 10-20]. Recently, layered TMDs (groups IVB-VIIB) mainly disulfides such as molybdenum disulfide (MoS_2), tungsten disulfide (WS_2), vanadium disulfide (VS_2),

niobium disulfide (NbS_2), tantalum disulfide (TaS_2), manganese disulfide (MnS_2); diselenides including titanium diselenide ($TiSe_2$), vanadium diselenide (VSe_2), molybdenum diselenide ($MoSe_2$), tungsten diselenide (WSe_2), manganese diselenide ($MnSe_2$); and tellurides like molybdenum ditelluride ($MoTe_2$), tungsten ditelluride (WTe_2) have fascinated widespread research interests and unveiled immense potential application in supercapacitors [8, 10, 12-13, 17, 21-23]. Among them, MoS_2 and WS_2, as a class of layered-structure with pseudo-capacitive merit, high mobility at room temperature, fast ion diffusion, larger interplaner spacing and specific capacitances, and also other various versatile properties, have been most commonly used in supercapacitors and under intensive investigation over the years [1, 3, 5-9, 20, 22]. However, MoS_2 and/or WS_2 nanostructures in the form of nanowires, nanoparticles, nanosheets, nanoworms, nanopetals and many others with high specific capacitances have already been synthesized by utilizing sophisticated instrumentation like *in situ* sulfuration, chemical vapour deposition, ionic liquid assisted exfoliation, hydrothermal process by adding surfactants, high temperature solution phase and self-propagating high-temperature methods [5-10, 14]. Since nanostructured MoS_2 and WS_2 are often being extremely difficult to prepare in low-cost, scalable production with controlled growth morphology, the alternate for a facile methodology is, therefore, relatively valuable. Consequently, it is challenging to synthesize MoS_2 and WS_2 nanostructures at low production cost with easy operation, one-step synthetic procedure and environmentally begin for high product purity as well as high yield industrial production.

Although MoS_2 and WS_2 nanostructures exhibit superior supercapacitor electrode performances but their poor electrical conductivity, complex preparation procedures and instability restrict their widespread use for supercapacitor application. On the other hand, conducting polymer especially polyaniline (PANi), which is promising for its high electrical conductivity suffer from low mechanical stability and poor cycle life. The combination of the nanostructured Mo/WS_2 with PANi is called nanocomposite. However, PANi combined with Mo/WS_2 nanostructures can enhance their performances and provide interesting properties. The development of new materials, therefore, is of paramount importance. Moreover, it is well accepted that the hydrothermal synthesis of polyaniline (PANi)-based composites with MoS_2 and/or WS_2 nanostructures is considered to be a great potential methodology to enhance the performance and properties of nanostructured MoS_2, WS_2 and/or PANI [24-25].

In this context, the present study systematically described three main thrusts on nanostructured MoS_2 and WS_2. The first thrust is associated with the facile, environmentally begin and cost-effective production of MoS_2 and WS_2 nanostructures via hydrothermal methodology with basic controlled formation mechanism. The second thrust elaborates a deep insight into distinctive electron microscopy (EM) including scanning EM (SEM), field-emission SEM (FESEM), transmission EM (TEM), scanning TEM (STEM) images of MoS_2 and WS_2 nanostructures with unusual 0D, 1D, 2D and 3D geometries. Further, the composite prepared by mechanical mixing of oxidative polymerization synthesized PANi and hydrothermal synthesized WS_2 nanorods and structurally characterized by SEM and FT-IR spectroscopy techniques. Third, impact of existing morphologies on supercapacitor performance of MoS_2 and WS_2 nanostructures is discussed and described detail. Based on the important findings, it is obvious that both MoS_2 and WS_2 nanostructured

materials detailed here will be a bright potential for applications in high-performance energy storage devices especially supercapacitors.

II. Synthesis of MoS_2 and WS_2 Nanostructures, PANi and Composite

A. Hydrothermal Synthesis of MoS_2 and WS_2 Nanostructures

Among various synthesis methods, the hydrothermal method is the most important method and is being extensively in practice for producing nanomaterials with novel morphologies. Nanostructured materials produced via hydrothermal synthesis method can be used for a broad range of potential applications including catalysis, biomedicine, smart electrochemical sensing and many other electronics, optoelectronics, optical biosensor devices. Hydrothermal method is an example of bottom-up approach and is the type of liquid phase preparation methodology developed by optimizing the thermodynamic variables, mainly temperature and pressure, of aqueous solution that dissolves and recrystallizes the required materials, which are relatively insoluble under ordinary conditions. The temperature is usually kept above 100 °C (but < 300 °C) and pressure above 1 atmosphere. Under these conditions, water plays two crucial roles as solvent for the reactants or precursors and pressure transmitting medium. In hydrothermal synthesis, the precursors are dissolved in water and heated above the boiling point in a sealed vessel (called the stainless-steel Teflon-lined autoclave) at ambient pressure. Moreover, as the synthesis is conducted in a closed reaction vessel, varied chemicals and starting materials can be recovered and reused, consequently making it an environmental-friendly synthesis methodology [6, 24]. This synthesis method is strongly depends on the heating medium and solubility of metal precursors in water under distinct pressure and/or temperature conditions. Different metal oxides (ZnO, $BaTiO_3$, Al_2O_3, TiO_2, VO_2, MoO_3, WO_3), layered oxides, layered sulfides (MoS_2, TiS_2, WS_2), elemental nanostructures (Bi, hBN) can be formed by this simple approach in the form of nanotubes, nanowires, nanoflowers and nanosheets. Interestingly, 2D crystals have low resistance for bending, the hydrothermal energy, therefore, curls the crystals in 2D nanostructures formation. The mechanism of hydrothermal synthesis, which is a liquid reaction-based approach, involves the chemical reaction of materials in aqueous solution which follows the solution nucleation model.

Hydrothermal method is highly effective and simplistic method with potential for mass production of functional MoS_2 and WS_2 nanomaterials in 0D, 1D, 2D and 3D for industrial applications. For example 0D nanostructures including nanodots and quantum dots, 1D nanostructures including nanofibers, nanowires, nanobelts and nanorods, 2D nanostructures including nanoplatelets and nanoarrays, and 3D nanostructures inclusing nanowalls, nanoflowers and nanodiamonds. The upper panel of Scheme 1 elucidates a schematic depiction for the formation mechanism of cauliflower-like MoS_2 nanostructure consisting of agglomerated nanowalls synthesized via hydrothermal approach [6]. The lower panel of Scheme 1 illustrates the schematic representation for the concept of 1D WS_2 nanorods synthesis method followed by hydrothermal approach [14]. Scheme 1 also demonstrates the hydrothermal reaction conditions at specify temperature (180 °C; the condition at which the formation started) for particular time (24 h; the parameter at which the formation completed). Interestingly, it was further confirms the successful preparation of MoS_2 nanoflowers and WS_2 nanorods via FESEM and TEM images, respectively.

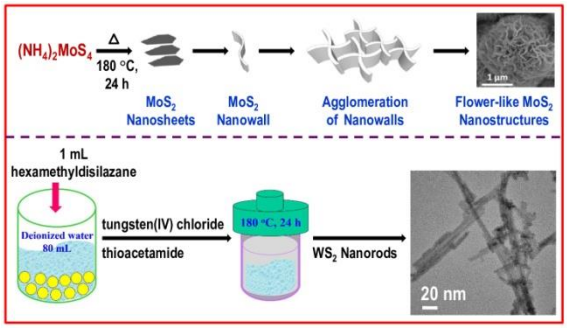

Scheme 1. Schematic illustration for the growth mechanism of 3D MoS_2 nanostructures (upper panel; Reproduced with permission from ref. 6, copyrights reserved to the American Chemical Society 2013) and concept of synthesis method of 1D WS_2 nanorods (lower panel; Reproduced with permission from ref. 14).

B. Preparation of PANi

PANi was prepared by a simple oxidative polymerization method within a short time. In a typical synthesis procedure, 0.25 M of aniline monomer was added in 1M HCl and ultrasonicated for 2 hours. To this solution 1M freshly prepared and precooled ammonium peroxydisulfate (APS; 20 mL) in 1M HCl was added dropwise for 30 minutes. The mixture was left for polymerization for 6 hours at 0-5 °C under constant stirring. The PANi was obtained by filtering and rinsing the reaction mixture with Millipore water and absolute methanol followed by drying the greenish black powder under vacuum at 60 °C for 24 hours. Methanol washing is desirable to remove the oligomeric impurities.

C. Preparation of PANi-WS_2 composite

PANi-WS_2 composite was prepared by mechanical mixing method. The as-prepared PANi was mixed with previously prepared WS_2 in different weight ratios (PANi:WS_2 weight ratios were 1:1, 3:1, and 5:1) in a DMF solvent by grinding them into a mortar-pestle for 2 hours. The homogenous mixture was then ultrasonicated for 3-4 hours to disperse and for better incorporation of WS_2 in the polymer matrix. After sonication, the mixture was magnetically stirred for 6-8 hours. The mixture was, finally then filtered off and washed with Millipore water and methanol for several times. The PANi-WS_2 composites were collected by drying the powder in oven at 60 °C for 12 hours.

III. Results and Discussion

A. Morphologies of MoS_2 and WS_2 Nanostructures

A.1. Zero-dimensional (0D) MoS_2 and WS_2 Nanostructures

Figure 1 illustrates the TEM images of 0D MoS_2 and WS_2 nanostructures. Figure 1(a) provides the TEM image of MoS_2 nanodots synthesized by hydrothermal method depicting the MoS_2 sample contains a large number of nanodots with almost uniform morphology. The size of MoS_2 nanodots varies in ranging from 2 nm to 8 nm with the maximum at about 5 nm. Figure 1(b) elucidates the TEM image of WS_2 nanodots synthesized via ionic liquid assisted grinding exfoliation method showing the dimension of nanodots of about 2 nm (as marked with white dotted circle). Figure 1(c) shows the TEM image of MoS_2 quantum dots (QDs) produced by hydrothermal method revealing the homogenously distributed spherical QDs with an average particle size of about 5 nm. Figure 1(d) displays the TEM image of WS2 QDs synthesized via hydrothermal route demonstrating the synthesized WS2 QD having size range from 8 nm to 20 nm with majority at about 12 nm.

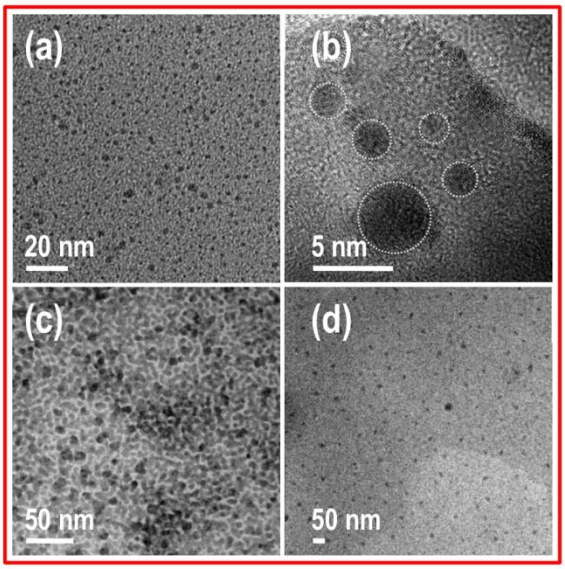

Figure 1. TEM images of (a) MoS_2 nanodots (Reproduced with permission from ref. 26, copyrights reserved to Chinese Physical Society 2018), (b) WS_2 nanodots (Reproduced with permission from ref. 2, copyrights reserved to The Royal Society of Chemistry 2017), (c) MoS_2 Quantum Dots (Reproduced with permission from ref. 27) and (d) WS_2 Quantum Dots (Reproduced with permission from ref. 28, copyrights reserved to The Royal Society of Chemistry 2020).

A.2. One-dimensional (1D) MoS_2 and WS_2 Nanostructures

Figure 2 demonstrates the electron microscopy (EM) images of 1D MoS_2 nanostructures. Figure 2(a) represents the low magnification transmission EM (TEM) image of MoS_2 1D-nanoribbons and the corresponding inset exhibits a close-up of one nanoribbon (as marked with red circle in main image), unveiling the clear straight and sharp edges. Figure 2(b) elucidates the SEM micrograph of MoS_2 nanotubes showing a narrow size distribution with a mean diameter of about 70 nm. Figure 2(c) shows the SEM image of MoS_2 nanofiber bundles synthesized by hydrothermal methodology clearly displaying the formation of bundles of well-dispersed MoS_2 nanofiber. Figure 2(d) provides the low magnification TEM image of MoS_2 nanobelts synthesized via chemical vapour deposition (CVD) method revealing a unique 1D geometry.

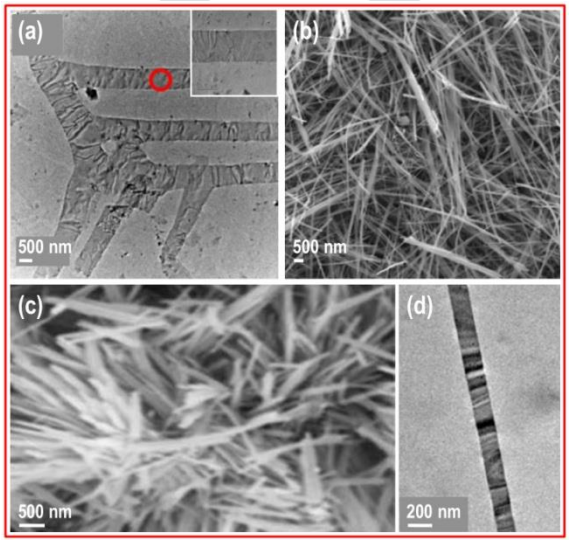

Figure 2. EM images of 1D MoS_2 nanostructures; (a) TEM image of nanoribbons (Reproduced with permission from ref. 10, copyrights reserved to Wiley 2019), (b) SEM image of nanotubes (Reproduced with permission from ref. 11, copyrights reserved to the American Chemical Society 2021), (c) SEM image of nanofiber bundles (Reproduced with

permission from ref. 21, copyrights reserved to Springer 2007) and (d) TEM image of nanobelts (Reproduced with permission from ref. 12, copyrights reserved to the American Chemical Society 2018).

Figure 3 elucidates the EM images of WS_2 nanostructures in different 2D geometries. Figure 3(a, b) displays the SEM image of WS_2 nanotubes grown in a vertical (fluidized-bed) reactor and horizontal reactor. From the SEM images, it is clear obvious that the distribution of diameters is larger for the nanotubes grown in vertical reactor than the nanotubes grown in horizontal reactor. Additionally, the WS_2 nanotubes grown in vertical reactor are longer and narrower with larger aspect ratio as compared to grown in horizontal reactor. Figure 3(c) depicts the WS_2 nanowires synthesized by sulfurization of tungsten oxide nanowires. Figure 3(d) provides a TEM image of WS_2 nanorods obtained by hydrothermal approach exhibiting a length within the range of 20-200 nm and a thickness of 3-6 nm.

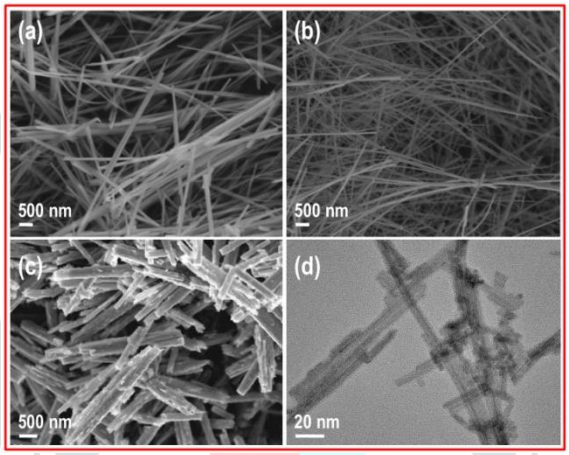

Figure 3. EM micrographs of 1D WS_2 nanostructures; SEM images of nanotubes grown by the scaled up in (a) vertical and (b) horizontal reactor (Reproduced with permission from ref. 11, copyrights reserved to the American Chemical Society 2021), (c) SEM image of nanowires (Reproduced with permission from ref. 13) and (d) TEM image of nanorods (Reproduced with permission from ref. 14).

A.3. Two-dimensional (2D) MoS_2 and WS_2 Nanostructures

Figure 4 displays the EM images of MoS_2 nanostructures with unique 2D geometries. Figure 4(a) represents a top-side FESEM image of vertically standing MoS_2 nanosheets demonstrating the nanosheets are uniformly grown on substrate. Figure 4(b) displays the SEM image of MoS_2 nanoribbon by synthesized by CVD method showing a smooth ribbon-like nanostructure with width of about 100 nm and length in several microns. Figure 4(c) illustrates the nanolamellar MoS_2 particles signifying the particles have width ranging between 100 nm and several micrometers. Figure 4(d) elucidates the top-view SEM image of MoS_2 nanoplatelets depicting uniformly sized and densely packed nanoplatelets and the thickness varies from 3 nm to 6 nm. Figure 4(e_1-e_2) indicates the SEM images of MoS_2 nanoflakes synthesized by two different approaches like liquid phase exfoliation and wet-chemical method.

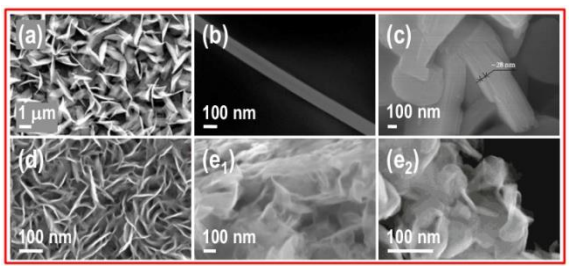

Figure 4. EM micrographs of 2D MoS_2 nanostructures; (a) top-view FESEM image of vertically standing nanosheets (Reproduced with permission from ref. 15), SEM images of (b) nanoribbon (Reproduced with permission from ref. 16, copyrights reserved to the American Chemical Society 2021), (c) nanolamellar (Reproduced with permission from ref. 29), (d) nanoplatelets (Reproduced with permission from ref. 17), and nanoflakes synthesized by liquid phase exfoliation method (e_1; Reproduced with permission from ref. 18) and wet-chemical process (e_2; Reproduced with permission from ref. 3).

Figure 5 provides the unique 2D geometries of WS_2 nanostructures. Figure 5(a) shows the FESEM image of WS_2 conical nanoarray obtained by a facile hydrothermal method at a large-scale view with an average width of about 200 nm. Figure 5(b) indicates the scanning TEM (STEM) image of single WS_2 conical tube that curled from WS_2 nanobelts. Figure 5(c) describes the high magnification SEM image of WS_2 nanoplates elucidating the hexagonal surface morphology, and the thickness range is 50-100 nm. Figure 5(d) presents the SEM micrograph of WS_2 nanoflakes signifying the particulate with a primary size ranges from 50 to 200 nm.

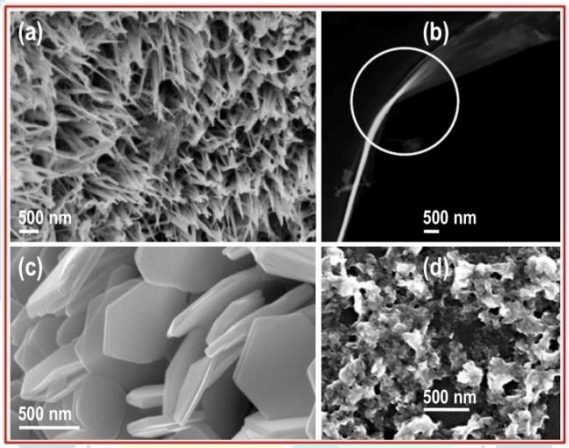

Figure 5. EM micrographs of 2D WS_2 nanostructures; (a) FESEM image of conical nanoarray, (b) STEM image of single screwed coin-like nanobelt (Reproduced with permission from ref. 30), SEM images of (c) hexagonal nanoplates (Reproduced with permission from ref. 22) and (d) nanoflakes (Reproduced with permission from ref. 4, copyrights reserved to Wiley 2014).

A.4. Three-dimensional (3D) MoS_2 and WS_2 Nanostructures

Figure 6 describes the SEM images of 3D MoS_2 nanostructures in different morphologies. Figure 6(a) demonstrates the SEM image of MoS_2 3D spherical structure exposing folded MoS_2 nanoslices in distinct directions to produce a peony structure. Figure 6(b) displays the SEM image of MoS_2 nanodiamonds appearing in polyhedron morphology with particle size in the range of 30-300 nm. Figures 6(c_1-c_4) elucidate MoS_2 3D flower-like morphology, which consisting of ultrathin 2D geometry especially nanosheets and/or nanopetals. Figure 6(c_1) indicates the SEM image of MoS_2 nanoflowers unveiling petal-like morphology with more faces and sharp edge sites. The distribution of particle size in nanoflowers varies between 0.5-1.0 μm. Figure 6(c_2) and Figure 6(c_3) depict FESEM images of an agglomerated rounded flower-like morphology equivalent to a pink carnation flower and marigold flower, respectively. The diameter of the flowers is observed to be about 700 nm and 2800 nm for respectively carnation and marigold flower-like MoS_2. Figure 6(c4) represents a SEM image of MoS_2 nanoflower exhibiting a compact nanoflower structure with a particle size around 1 μm. Figure (d_1) illustrates the 3D morphology of MoS_2 expressing a flower-like

morphology containing nanowall petals. Figure 6(d2) provides the field-emission gun SEM (FEG-SEM) image of MoS_2 illustrating the agglomerated cauliflower morphology consisting of flake/wall type morphology (Figure 6(e)) of MoS_2 and the wall thickness varies from 19-23 nm (as marked by solid yellow arrows in Figure 6(e)).

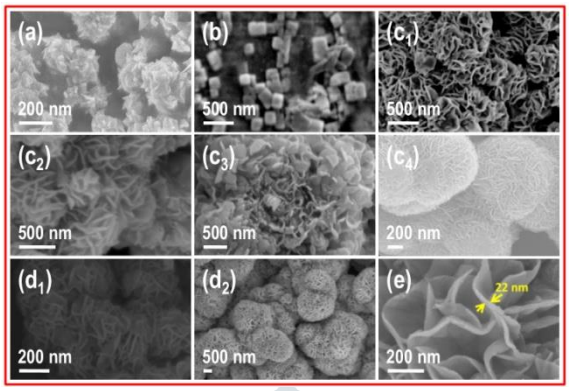

Figure 6. EM micrographs of 3D MoS_2 nanostructures; SEM images of (a) spherical structure consisted of nanoslices (Reproduced with permission from ref. 31, copyrights reserved to Wiley 2020), (b) nanodiamond and (c_1) nanoflowers (Reproduced with permission from ref. 32), (c_2) carnation flower-like and (c_3) marigold flower-like (Reproduced with permission from ref. 33, copyrights reserved to Elsevier 2022), (c_4) nanoflower (Reproduced with permission from ref. 5), (d_1) nanowalls (Reproduced with permission from ref. 7), (d_2) cauliflower and (e) nanowalls morphology (Reproduced with permission from ref. 6, copyrights reserved to the American Chemical Society 2013).

The EM images of 3D WS_2 nanostructures are presented in Figure 7(a-d). Figure 7(a) displays the SEM image of WS_2 nanoflowers with an average size/diameter of about 1 μm consisting of well-arranged nanopetals. Figure 7(b) reveals the top-view SEM image of WS_2 nanowall with a height of about 190 nm. Figure 7(c) demonstrates the SEM image of WS_2 nanoparticles elucidating a hexagonal layered-structure with a smooth surface. From the Figure 7(c) it is clear visible that the length and width dimensions are relatively much larger than the thickness dimension with an average particle size of about 80 nm. Figure 7(d) shows the morphology of WS_2 nanotriangles that are accumulated in a 3D orientation.

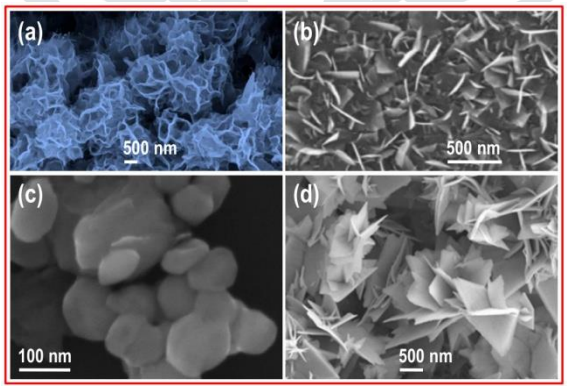

Figure 7. EM micrographs of 3D WS_2 nanostructures; SEM images of (a) nanoflowers (Reproduced with permission from ref. 8, copyrights reserved to the American Chemical Society 2019), (b) top-view of nanowalls (Reproduced with permission from ref. 23, copyrights reserved to the American Chemical Society 2020), (c) nanoparticles (Reproduced with permission from ref. 34) and (d) FESEM image of nanotriangles (Reproduced with permission from ref. 19).

B. Analyses of WS_2, PANi and PANi-WS_2 Nanocomposite

The SEM images of nanostructured WS_2, PANi and PANi-WS_2 composite are depicted in Figures 8((a)-(c)). The SEM image of PANi (Figure 8(a)) represents the agglomerated regularly arranged granular morphology.

Figure 8(b) displays the rod-like morphology of WS_2 nanostructures with good homogeneity. Figure 8(c) illustrates the SEM image of PANi-WS_2 nanocomposite elucidating the agglomerated granular morphology in which WS_2 nanorods is embedded in PANi matrix [35]. Figure 8(d) provides the FT-IT spectrum of the as-obtained PANi in the range of 500-4000 cm^{-1}. The characteristics bands were obvious at 3723, 3214, 2895, 2341, 2085, 1838, 1558, 1442, 1288, 1087 and 785 cm^{-1}. The bands appeared at high wavenumbers, 3723, 3214 and 2895 cm^{-1} correspond to N-H stretching and C-H stretching, respectively of aromatic amines. The bands in wavenumber ranging 2000-2400 cm^{-1} observed at 2341, and 2085 cm^{-1} were related to O=C=O stretching of CO_2 and C-H bending of aromatic compound, respectively. Bands obtained at 1838, 1558, 1442, 1228, 1087 and 785 cm^{-1} can be assigned to C=O stretching of anhydride, C=C stretching of quinonoid ring, C=C stretching of benzenoid ring, $C\text{-}N^+$ stretching, C-O stretching and C-H bending vibrations, respectively [36].

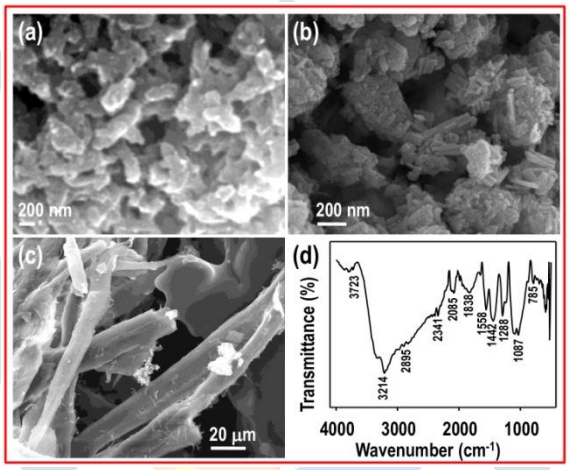

Figure 8. SEM micrographs of (a) PANi, (b) WS_2 nanorods and (c) PANi-WS_2 nanocomposite, the FT-IR spectrum (d) of PANi.

C. Morphology Effect on Supercapacitor Performance

Nowadays, development of MoS_2 and WS_2 nanostructures is attracting much attention due to their fascinating properties and versatility in several research areas including as solid lubricants, light-emitting substances, hydrogen storage media, wear resistance, electrode materials in supercapacitors, photochemical catalysts, and thermal- as well as optical-sensors. Most of applications utilize their unusual surface and structural properties, which are strongly depends on a variety of structural arrangements, shape, size and crystalline quality. Amongst various tremendous properties, research on supercapacitor performance of MoS_2 and WS_2 nanostructures has achieved an enormous interest in recent years due to their earth abundance, varied structure-phase availability and nontoxicity. For supercapacitors, surface morphology and phase tunability of MoS_2 and WS_2 nanostructures demonstrated the pivotal role in improving the supercapacitor performance especially specific capacitance by providing more active surface area reactive sites. Figure 8 shows the histograms describing a comparative study of the best results reported formerly on specific capacitance values of MoS_2 and WS_2 with distinctive 1D, 2D and 3D geometries. The higher specific surface area and/or active sites could be attributed to the higher specific capacitance values of MoS_2 nanostructures than that of WS_2 nanostructures, as obvious and denoted by numeric digits superscripted by comma symbol in Figure 9.

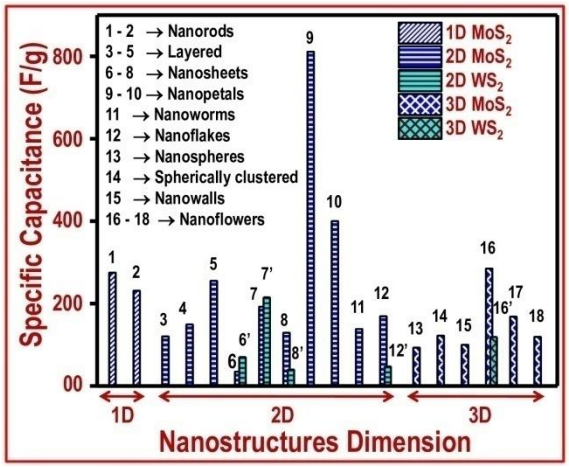

Figure 9. Histograms elucidating a comparative study of specific capacitance values for different MoS_2 and WS_2 nanostructures. The numeric symbol marked by comma superscript (as 6', 7', 8', 12' and 16') indicates the corresponding WS_2 nanostructures.

IV. Conclusion

In this study, three main thrusts on MoS_2 and WS_2 nanostructures are focused and described in detail. The first thrust is related to the facile, environmentally begin and cost-effective production of MoS_2 and WS_2 nanostructures synthesized by hydrothermal methodology with understanding of formation mechanism. A deep insight into structure-property relationship through expressing distinctive electron microscopy images of MoS_2 and WS_2 nanostructures with unique 0D, 1D, 2D and 3D geometries is the second thrust of this study. Moreover, structural characterizations were carrioud out by SEM and FT-IR spectroscopy techniques of composite synthesized by mechanical mixing of oxidative-polymerized PANi and hydrothermal-synthesized WS_2 nanorods. The third thrust is the analysis of impact of distinct morphologies on supercapacitor performance of MoS_2 and WS_2 nanostructures. We hope that the important findings on MoS_2 and WS_2 based nanostructured materials elaborated well here will be a great promising potential for further applications.

Acknowledgements

The author JG is thankful to the Science and Engineering Research Board, Department of Science and Technology (SERB-DST), New Delhi, Government of India for providing financial support through sponsored project ECR/2017/000879 (Diary No./Finance No. SERB/F/7840/2018-2019).

Conflict of Interest

The authors declare no conflict of interest.

References

[1] Zhang, Z.; Wu, S.; Cheng, J.; Zhang, W. *Energy Storage Materials*, **2018**, *15*, 65-74. DOI: 10.1016/j.ensm.2018.03.013.

[2] Liu, W.; Benson, J.; Dawson, C.; Strudwick, A. et. al. *Nanoscale*, **2017**, *9*, 13515. DOI: 10.1039/c7nr04790h.

[3] Nguyen, T.M.N.; Vuong D.V.; Phong, M. T.; Le T. V. *Journal of Nanomaterials*, **2019**, *2019*, 8364740. DOI: 10.1155/2019/8364740.

[4] Cheng, L.; Huang, W.; Gong, Q.; Liu, C. et. al. *Angew. Chem. Int. Ed.*, **2014**, *53*, 1. DOI: 10.1002/anie.201402315.

[5] Jia, M.; Qi, T.; Yuan, Q.; Zhao, P. et. al. *Nanomaterials*, **2022**, *12*, 2006. DOI: 10.3390/nano12122006.

[6] Sen, U. K.; Mitra, S. *ACS Appl. Mater. Interfaces*, **2013**, *5*, 1240. DOI: 10.1021/am3022015.

[7] Sari, F.N.I.; Ting, J.M. *Scientific Reports*, **2017**, *7*, 5999. DOI: 10.1038/s41598-017-05805-z.

[8] Srinivaas, M.; Wu, C.Y.; Duh, J.G.; Wu, J.M. *ACS Sustainable Chem. Eng.* **2019**, *7*, 10363. DOI: 10.1021/acssuschemeng.9b00351.

[9] Pomerantseva, E.; Bonaccorso, F.; Feng, X.; Cui, Y. et. al. *Science*, **2019**, *366*, 969. DOI: 10.1126/science.aan8285.

[10] Wu, D.; Shi, J.; Zheng, X.; Liu, J. et. al. *Phys. Status Solidi RRL*, **2019**, *13*, 1900063. DOI: 10.1002/pssr.201900063.

[11] Sinha, S.S.; Yadgarov, L.; Aliev, S.B.; Feldman, Y. et. al. *J. Phys. Chem. C*, **2021**, *125*, 6324. DOI: 10.1021/acs.jpcc.0c10784.

[12] Murthy, A.A.; Li, Y.; Palacios, E.; Li, Q. et. al. *ACS Appl. Mater. Interfaces*, **2018**, *10*, 6799. DOI: 10.1021/acsami.7b16892.

[13] Asres, G.A.; Dombovari1, A.; Sipola1, T.; Puskás, R. et. al. *Scientific Reports*, **2016**, *6*, 25610, DOI: 10.1038/srep25610.

[14] Mishra, R.K.; Kumar, V.; Trung, L.G.; Choi, G.J. et. al. *Sensors*, **2022**, *22*, 8609. DOI: 10.3390/s22228609.

[15] Li, H.; Wu, H.; Yuan S,; Qian, H. *Scientific Reports*, **2016**, *6*, 21171. DOI: 10.1038/srep21171.

[16] Li, Z.; Jiang, Z.; Zhou, W.; Chen, M. et. al. *Inorg. Chem.*, **2021**, *60*, 1991. DOI: 10.1021/acs.inorgchem.0c03478.

[17] Jagminas, A.; Niaura, G.; Žalnėravičius, R.; Trusovas, R. et. al. *Scientific Reports*, **2016**, *6*, 37514. DOI: 10.1038/srep37514.

[18] Sun, J.; Li, X.; Guo, W,; Zhao, M. *Crystals*, **2017**, *7*, 198; DOI: 10.3390/cryst7070198.

[19] Minezaki, T.; Krüger, P.; Annanouch, F. E.; Cháfer, J. C. et. al. *Sensors*, **2023**, *23*, 4623. DOI: 10.3390/s23104623.

[20] Shelke, N.T.; Karche, B.R. *Journal of Alloys and Compounds*, **2015**, *653*, 298-303. DOI: 10.1016/j.jallcom.2015.08.255.

[21] Nagaraju, G.; Tharamani, C.N.; Chandrappa, G.T.; Livage, *J. Nanoscale Res. Lett.*, **2007**, *2*, 461. DOI: 10.1007/s11671-007-9087-z.

[22] Zhang, X.; Wang, J.; Xu, H,; Tan, H. et. al. *Nanomaterials*, **2019**, *9*, 840. DOI: 10.3390/nano9060840.

[23] Tang, S.Y.; Yang, C.C.; Su, T.Y.; Yang, T.Y. et. al. *ACS Nano*, **2020**, *14*, 10, 12668. DOI: 10.1021/acsnano.0c01264.

[24] Shandilya, M.; Rai, R.; Singh, J. *Advances in Applied Ceramics*, **2016**, *115*, 354-376 DOI: 10.1080/17436753.2016.1157131.

[25] Zhang, W. L.; Jiang, D.; Wang, X.; Hao, B.N. et. al. *J. Phys. Chem. C*, **2017**, *121*, 4989-4998. DOI: 10.1021/acs.jpcc.6b11656.

[26] Sui, L.; Jiang, Y.; Chen, A,; Song, J.C. et. al. *Chinese Journal of Chemical Physics*, **2018**, *31*,277. DOI: 10.1063/1674-0068/31/cjcp1802018.

[27] Roy, S.; Sharma S.; Chappanda N.K.; Chakraborty C. *Designs*, **2023**, *7*, 13, DOI: 10.3390/designs7010013.

[28] Mani, N.P.; Cyriac, J. *New J. Chem.*, **2020**. *44*, 10840. DOI: J. 10.1039/c9nj06159b.

[29] An, V.; Irtegov, Y.; Izarra, C.D. *Journal of Nanomaterials*, **2014**, *2014*, 865839, DOI: 10.1155/2014/865839.

[30] Xie, L.; Wang, L.; Zhao, W.; Liu, S. *Nature Communications*, **2021**, *12*, 5070. DOI: 10.1038/s41467-021-25381-1.

[31] Jiang, J.; Shen, Q.; Xue, P.; Qi, H. *Chemistry Select*, **2020**, *5*, 354. DOI: 10.1002/slct.201903924.

[32] Chen, Y.; Xiong, X.; Chen, Y.; Chen, L. et. al. *Biosensors*, **2023**, *13*, 506. DOI: 10.3390/bios13050506.

[33] Kumar, N.; Borkar, H.; Siroha, P.; Kumar, R. et. al. *Sensors & Actuators: B. Chemical*, **2022**, *372*, 132572. DOI: 10.1016/j.snb.2022.132572.

[34] Zhang, H.; Mo, Y.; Lv, J.; Wang, J. *Lubricants*, **2023**, *11*, 259. DOI: 10.3390/lubricants11060259.

[35] Megha, R.; Ravikiran, Y.T.; Kumari, S.C.V.; Chandrasekhar, T. et. al. *Polymer Composites*, **2018**, *39*, 3545-3555. DOI: 10.1002/pc.24375.

[36] Cui, S.; Wang, J.; Wang, X. *RSC Adv.*, **2015**, *5*, 58211-58219. DOI: 10.1039/C5RA06388D.